Geomorphology 253 (2016) 94–109

Contents lists available at ScienceDirect

Geomorphology

journal homepage: www.elsevier.com/locate/geomorph

Dynamic meandering in response to upstream perturbations and floodplain formation

F. Schuurman [a,b,*], Y. Shimizu [c], T. Iwasaki [d], M.G. Kleinhans [a]

[a] Department of Physical Geography, Faculty of Geosciences, Utrecht University, Utrecht, The Netherlands
[b] Department of Rivers, Deltas and Coasts, Royal HaskoningDHV, Amersfoort, The Netherlands
[c] Laboratory of Hydraulic Research, Graduate School of Engineering, Hokkaido University, Sapporo, Japan
[d] Department of Civil and Environmental Engineering, University of Illinois Urbana-Champaign, Urbana, IL, USA

ARTICLE INFO

Article history:
Received 23 October 2014
Received in revised form 24 April 2015
Accepted 2 May 2015
Available online 18 September 2015

Keywords:
Meandering
Meander model
Alternate bars
Floodplain
Perturbation

ABSTRACT

River meandering results from spatially alternating bank erosion and bar growth. Recent flume experiments and theory suggest that a continuous inflow perturbation is a requirement for sustained meandering. Furthermore, flume experiments suggest that bar–floodplain conversion is an additional requirement. Here, we tested the effects of continuous inflow perturbation and bar–floodplain conversion on meander migration using three numerical morphodynamic models: a 1D-model, and two 2D-models with one of them using adaptive moving grid. We focused on the interaction between bars and bends that leads to meander initiation, and the effect of different methods to model bank erosion and floodplain accretion processes on meander migration. The results showed that inflow perturbations have large effects on meander dynamics of high-sinuosity channels, with strong excitation when the inflow is periodically perturbed. In contrast, inflow perturbations have rather small effect in low-sinuosity channels. Steady alternate bars alone are insufficient to cause high-sinuosity meandering. For high-sinuosity meandering, bar–floodplain conversion is required that prevents chute-cutoffs and enhances flow asymmetry, whilst meandering with chute-cutoffs requires merely weak floodplain formation, and braiding occurs without floodplain formation. Thus, this study demonstrated that both dynamic upstream inflow perturbation and bar–floodplain conversion are required for sustained high-sinuosity meandering.

1. Introduction

River meandering (Fig. 1) is a well-studied subject in fluvial morphology with a long history of literature about the cause, processes and prediction of meandering. Nevertheless, the cause or causes of meander initiation and the necessary conditions for sustained meander migration are still topics of debate. Below we briefly review the combination of factors that is thought to be conducive to meandering, in particular the formation of alternate bars, the formation of floodplains, bend-cutoffs and upstream perturbations of curvature.

In the past, alternate bars formed by intrinsic instability have been credited to cause meander bend initiation in straight channels (e.g. Parker, 1976). However, these bars commonly have wavelengths several times smaller than meanders and migrate too fast to initiate meandering (Olesen, 1983; Blondeaux and Seminara, 1985; Whiting and Dietrich, 1993), with evidence also in nature (Fig. 1d, e). In contrast, forced alternate bars, induced by a steady instability such as a groin, seepage or meander bend, are able to initiate meandering (e.g. Ikeda et al., 1981; Blondeaux and Seminara, 1985; Struiksma and Crosato, 1989; Hall, 2004; Crosato and Mosselman, 2009). Alternatively, initial channel curvature has been used to start meandering in flume experiments and modeling (e.g. Duan and Julien, 2005; Asahi et al., 2013). Sustained meander migration, however, requires a sustained dynamic perturbation on the upstream boundary, as found in highly simplified linearized meander migration modeling (Lanzoni and Seminara, 2006). Without a dynamic perturbation, a meandering channel would return to its original state without bends, similar to a propagating wave. This was partly confirmed by flume experiments of Van Dijk et al. (2012), who showed that meander migration rates gradually decline in case of a static inflow perturbation, whereas meander migration continues in case of a dynamic inflow perturbation. However, such flume experiments usually only have the length of a few meanders, which is perhaps too short to enable internal perturbations to emerge and drive further meandering. Furthermore, the question remains how far downstream the effect of upstream perturbation propagates, because the characteristic downstream distance of influence of a perturbation in a meandering river is relatively short (Struiksma et al., 1985). Also, linear analyses showed that a straight channel with erodible bed and turbulent flow is intrinsically unstable, which results in bars and bends without the need for an external forcing (Struiksma et al., 1985;

* Corresponding author at: Department of Rivers, Deltas and Coasts, Royal HaskoningDHV, The Netherlands.
E-mail address: filip.schuurman@rhdhv.com (F. Schuurman).

http://dx.doi.org/10.1016/j.geomorph.2015.05.039
0169-555X/

Fig. 1. Examples of a. high-sinuosity meandering river characterized by abundance of vegetation along the river, a lack of bars, and neck-cutoffs (Rio Purus, Brazil); b. low-sinuosity meandering river with low vegetation density and chute-cutoffs (Allier, France); c. meandering river with bars forced by channel curvature (Wabash River, USA); d. meander bend with free bars, including mid-channel bars (Rio Parnaiba, Brazil); e. low-sinuosity river with free alternate bars (Cross River, Nigeria); f. asymmetrical shape of the alternate bars with bar-tail limbs at the downstream (Indus River, Pakistan). Flow in all examples is from left to right.
Source: Bing Maps (c, d, f) and Google Earth (a, b, e).

Blondeaux and Seminara, 1985). Thus, here we test whether a dynamic perturbation is indeed required for sustained meander migration and cutoff dynamics, using a situation with sufficient length.

Another requirement for meandering is a single-threaded channel without mid-channel bars, a conditions met within a limited range of relatively low width-depth ratios (e.g. Engelund and Skovgaard, 1973; Fredsoe, 1978; Crosato and Mosselman, 2009; Kleinhans and Van den Berg, 2011). The width-depth ratio in meandering rivers depends on the balance between bank erosion and inner bend accretion rates. Many meandering rivers have rather constant and uniform channel widths even though the channel migrates (Parker et al., 2011). This implies a dynamic equilibrium between bank erosion and bar growth in the inner bend, called 'bank pull' and 'bar push' by Parker et al. (2011), Eke et al. (2014) and Van de Lageweg et al. (2014), exists, despite bank erosion and bar growth have different underlying processes. It might justify the application of constant and uniform channel width in the classical one-dimensional meander migration models of Ikeda et al. (1981), Howard and Knutson (1984), Parker and Andrews (1986), Crosato (1987), Johannesson and Parker (1989) and Sun et al. (1996). However, recent modeling and flume experiments demonstrated that equilibrium channel width is only achieved by additional processes to reduce bank erosion rates or increase inner bend accretion rates (Dulal et al., 2010; Parker et al., 2011; Van Dijk et al., 2013b). Acceleration of inner bend accretion is, for example, achieved by vegetation encroachment to convert the inner bend bars into floodplain (Gran and Paola, 2001; Erskine et al., 2009; Tal and Paola, 2010; Erskine et al., 2011; Van Dijk et al., 2013a; Iwasaki et al., 2015), Fig. 1b), hereafter called 'bar–floodplain conversion'.

Numerical two-dimensional morphodynamic meander models have been using a variety of methods to compute bank erosion and bar–floodplain conversion (e.g. Mosselman, 1995; Parker et al., 2011; Asahi et al., 2013; Nicholas, 2013). Despite their large differences, most of these models were able to produce high-sinuosity meandering with nearly uniform and constant channel width. However, many two-dimensional meander models have been applied on laboratory scale. The bar–floodplain conversion rules in these models ignored time scale differences between bed evolution (i.e. sand transport, bar dynamics) and bar–floodplain conversion (i.e. vegetation encroachment, deposition of fine cohesive sediment on the pointbars). This would render these models useless for 'real world' rivers.

Bend-cutoffs are well-known to be critical aspects of meander dynamics, with neck-cutoffs reducing the sinuosity of high-sinuosity meanders (Fig. 1a, c; e.g. Hooke, 2004; Camporeale et al., 2008). Chute-cutoffs in high-sinuosity rivers result in a minor decrease of sinuosity (Grenfell et al., 2014), but in low-sinuosity channels, they may prevent high-sinuosity (Fig. 1f; Howard, 1996; Constantine et al., 2010) and lead to potential braiding (Fig. 1b; Sarker and Basumallick, 1968; Grenfell et al., 2012; Van Dijk et al., 2012). Most numerical meander migration models can model either neck-cutoffs or chute-cutoffs, but not both. This is, among others, because of a dynamic boundary-fitted grid, which automatically removes the inner bend bars from the computational domain and thus disable chute-cutoffs, or because the model assumes a simplified transverse bed profile. At the same time, models without boundary-fitted grid might overestimate channel widening and chute-cutoffs. A solution is application of different models for the same case to investigate meander dynamics.

The objective of this chapter is to determine the necessary and sufficient conditions for meander initiation and sustained meander migration. In order to accomplish this objective, we a) determined the effect of inflow perturbations on meander initiation and meander dynamics, i.e. growth, migration and cutoff, b) analyzed the interaction between bed deformation (bars) and channel deformation (meander bends), and c) determined the contribution of bank erosion and bar–floodplain conversion to meander dynamics. We conducted simulations with two

state-of-the-art numerical models and one classical Ikeda-Parker (IP) model. The differences between these models (Table 1), in particular the processes for bank erosion and bar–floodplain conversion, allow us to infer the necessary and sufficient conditions for meander initiation and sustained meander migration.

This chapter is organized as follows: it starts with a brief description of the models and the method for analyses. Next, we describe the model results of the meandering using a dynamic upstream inflow perturbation, similar to Van Dijk et al. (2012), and with static and no inflow perturbation. We do this in the sequence Delft3D (Schuurman et al., 2013), Nays2D (Asahi et al., 2013) and the IP-model (Ikeda et al., 1981). After this, we compare the methods of modeling bank erosion and bar–floodplain conversion in the models, and their effects on the meander dynamics. Subsequently, we analyze in more detail the interactions between bends and bars, both forced and free migrating bars. We finalize with a discussion about the necessary and sufficient conditions for meander initiation and sustained meander migration, and give the main conclusions.

2. Model description

2.1. Background

Delft3D computes two or three-dimensional hydrodynamics, sediment transport and bed level change. For sake of computational efficiency, we applied the two-dimensional flow mode with parameterization of spiral flow on sediment transport. A standard version of Delft3D (version 3.28) was used. Delft3D has been applied in many scientific projects for river systems (e.g. Crosato and Saleh, 2010; Schuurman et al., 2013; Van Dijk et al., 2014; Schuurman and Kleinhans, 2015). Furthermore, Delft3D has proven to be reliable and accurate in the demanding practice of river engineering.

Nays2D is a two-dimensional model with parameterization of the spiral flow. Besides sediment transport and bed level change, it computes bank erosion and bar–floodplain conversion, and adjusts the grid boundaries according to the bank erosion and bar–floodplain conversion rates, a method also used by Olsen (2003) and Duan and Julien (2010). After adjustment of the grid boundaries, it redistributes the grid cells to regain orthogonality. Nays2D accounts for neck-cutoffs, which occurs when two channel reaches intersect. Nays2D was developed at Hokkaido University (Japan), and has been applied to simulate meander dynamics in flume experiments (Dulal et al., 2010; Asahi et al., 2013).

The IP-model is a one-dimensional model based on the classical and often applied model of Ikeda et al. (1981) extended by Johannesson and Parker(1989). The specific code used in this study was developed at Utrecht University with the purpose to model meander migration of intertidal creeks (Kleinhans et al., 2009).

Because of important differences in numerics, modeled processes, settings and schematization, one should be careful with directly comparing the results of the three models. Instead, the three models were regarded as complementary. Thus, we mainly compared between the different scenarios in each model separately.

Table 1
Model comparison.

Parameter	Delft3D	Nays2D	IP-model
Grid	Curvilinear[a]	Curvilinear	Nodes
Hydrodynamics	2D/3D[b]	2D	1D
Regridding	No	Yes	Yes
Bar dynamics	Yes	Yes	No
Bank erosion	Yes	Yes	Yes
Bank stability	No	Yes	No
Bar–floodplain conversion	No	Yes	Yes[c]

[a] In this study, a rectangular grid was used.
[b] In this study, only 2D flow was used.
[c] Bar–floodplain conversion rate equals bank erosion rate.

2.2. Hydrodynamics

The hydrodynamics in Delft3D and Nays2D are modeled by applying conservation of momentum (Eqs. (1) and (2)) and mass (Eq. (3)), assuming hydrostatic pressure:

$$\frac{\partial u}{\partial t}+u\frac{\partial u}{\partial s}+v\frac{\partial u}{\partial n}+g\frac{\partial z_w}{\partial s}+\frac{gu\sqrt{u^2+v^2}}{C^2h}-V\left(\frac{\partial^2 u}{\partial s^2}+\frac{\partial^2 u}{\partial n^2}\right)+F_s=0 \quad (1)$$

$$\frac{\partial v}{\partial t}+u\frac{\partial v}{\partial s}+v\frac{\partial v}{\partial n}+g\frac{\partial z_w}{\partial n}+\frac{gv\sqrt{u^2+v^2}}{C^2h}-V\left(\frac{\partial^2 v}{\partial s^2}+\frac{\partial^2 v}{\partial n^2}\right)+F_n=0 \quad (2)$$

$$\frac{\partial h}{\partial t}+\frac{\partial}{\partial s}hu+\frac{\partial}{\partial n}hv=0 \quad (3)$$

where s is the streamwise coordinate (m), n is the transverse coordinate (m), z_w is the free water surface level (m), u is the depth-average flow velocity in s-direction (m/s), v is the depth-average flow velocity in n-direction (m/s), h is the water depth (m), C is the Chézy roughness ($m^{0.5}/s$), g is the gravity acceleration constant (m/s^2), V is the horizontal eddy viscosity (m^2/s) and $F_{s,n}$ is the acceleration term due to stream line curvature (m/s^2). The vertical flow is parameterized in order to include the effect of streamline curvature induced spiral flow. The turbulence closure is solved by applying a constant uniform horizontal eddy viscosity of 1 m^2/s.

Nays2D and Delft3D solve Eqs. (1) to (3) using finite difference methods on a structured curvilinear grid. Delft3D uses an ADI-method, which splits each time step in two parts: one to solve for the s-direction and one to solve for the n-direction. Nays2D uses the CIP-method, which splits each time step in one half to solve the non-advective part and one half to solve the advective part. A detailed description of the model numerics can be found in Asahi et al. (2013) for Nays2D, and in Deltares (2009) and Schuurman et al. (2013) for Delft3D.

The IP-model uses linearized hydrodynamics, with uniform and constant values for cross-sectional averaged flow velocity U (m/s), water depth and channel width W (m). The excess flow velocity in the outer bend u_b (m/s), which is the difference between the outer bend flow velocity and cross-sectional average flow velocity, is computed based on local channel curvature K (rad/m) and a phase lag (Edwards and Smith, 2002):

$$\frac{\partial u_b}{\partial s}+\frac{u_b}{\lambda_w}=U\frac{W}{2}\left(-\frac{\partial K}{\partial s}+\frac{PK}{\lambda_w}\right) \quad (4)$$

with P defined as:

$$P=\frac{F^2+A_n+A_s-1}{2} \quad (5)$$

and λ_w (m) is the flow adaptation length:

$$\lambda_w=\frac{hC^2}{2g} \quad (6)$$

where A_n is a transverse bed slope coefficient, A_s is a downstream momentum redistribution coefficient, F is Froude number, C is the Chézy roughness ($m^{0.5}/s$) and g is the gravity acceleration constant (m/s^2). Following Kleinhans et al. (2009), we used $A_n=6$, and $A_s=130(2h/W)^2$. The flow adaptation length introduces a spatial phase lag between channel curvature and bank erosion. This model assumes an equilibrium longitudinal bed elevation profile, which implies no sediment transport gradient in downstream direction.

2.3. Sediment transport in Delft3D and Nays2D

In Delft3D and Nays2D, sediment transport rates are equal to the sediment transport capacity, computed using Engelund and Hansen (1967):

$$q_{tot} = \frac{0.05U^5}{\sqrt{g}C^3\Delta^2 D_{50}} \tag{7}$$

where q_{tot} is the total sediment transport per unit width in streamline direction (m^2/s), U is the depth-average flow velocity in streamline direction, Δ is the relative density of submerged sediment (−) and D_{50} is the median grain size (m).

In Delft3D, the effect of spiral flow on the sediment transport direction is parameterized by:

$$\tan(\phi_\tau) = -A\frac{h}{R} \tag{8}$$

where ϕ_τ is the angle between the streamline direction and the sediment transport direction, h is the water depth (m), R is the radius of the local streamline curvature (m), κ is the Von Karman constant (0.41) and the spiral flow coefficient A, assuming a logarithmic flow velocity profile, is given by:

$$A = \frac{2}{\kappa^2}\left[1 - \frac{1}{2}\frac{\sqrt{g}}{\kappa C}\right]. \tag{9}$$

The sediment transport rates are corrected for the bed slope by using Talmon et al. (1995):

$$q_s = q_{tot}\left[\cos(\phi_\tau) - f(\theta)\frac{\partial z_b}{\partial s}\right] \tag{10}$$

$$q_n = q_{tot}\left[\sin(\phi_\tau) - f(\theta)\frac{\partial z_b}{\partial n}\right] \tag{11}$$

where q_s is the total sediment transport in s-direction (m^2/s), q_n is the total sediment transport in n-direction (m^2/s) and where.

$$f(\theta) = \frac{1}{\alpha\theta^\beta} \tag{12}$$

in which α and β are calibration parameters. As we had no validation data, we applied $\alpha = 0.7$ and $\beta = 0.5$, adopted from Schuurman et al. (2013).

In Nays2D, the effects of spiral flow and transverse bed slope effect are parameterized by:

$$q_n = q_{tot}\left[\frac{v}{\sqrt{u^2+v^2}}\frac{h}{R}N - f(\theta)\frac{\partial z_b}{\partial n}\right] \tag{13}$$

in which the first term is to account for the spiral flow with N being a calibration parameter for spiral flow intensity, and the second term is to account for transverse bed slope effect (Hasegawa, 1981), with.

$$f(\theta) = \sqrt{\frac{\theta_c}{\mu_s\mu_k\theta}} \tag{14}$$

where the static coefficient of Coulomb friction $\mu_s = 1.0$ and the dynamic coefficient of Coulomb friction $\mu_k = 0.45$, adopted from Jang and Shimizu (2005). For comparison with Eq. (12), parameter α has the same effect as $\sqrt{(\mu_s\mu_k)/\theta_c}$ and β is 0.5 in both models. For a grain size of 2.0 mm, $\theta_c = 0.041$ and thus $\sqrt{(\mu_s\mu_k)/\theta_c} = 3.3$. This means that the transverse bed slope effect in Nays2D is smaller than in the Delft3D-simulations. For spiral flow, we used $N = 13$ as default, and determined its effect on the meander pattern in a sensitivity analysis.

In both Delft3D and Nays2D, the bed level is updated after each time step using the Exner equation, which ensures mass conservation of sediment:

$$\frac{dz_b}{dt} = MorFac\left[\frac{\partial q_s}{\partial s} + \frac{\partial q_n}{\partial n}\right] \tag{15}$$

in which $MorFac$ is an acceleration factor, which reduces computational time. In Delft3D, we applied $MorFac = 25$; in Nays2D we applied $MorFac = 50$. Usually, the effect of the acceleration factor on the morphology is small (Roelvink, 2006; Crosato et al., 2011; Schuurman et al., 2013). In order to increase numerical stability, we applied in Nays2D a non-erodible bed layer $z_{b,\min} = -8$ m, and determined the sensitivity to this parameter.

2.4. Bank erosion and bar–floodplain conversion

In Delft3D, bank erosion is implemented by coupling horizontal bank retreat to bed degradation. Bank erosion occurs between an inundated grid cell and a dry grid cell, thus not restricted to the outer banks. Incision of the inundated grid cell is equally divided over both grid cells, thus lowering both the dry and wet grid cells. This process can continue until the dry grid cell is inundated.

Bar–floodplain conversion in Delft3D is not computed explicitly. However, in scenarios D3D-C5 and D3D-C6 we applied a simple vegetation growth rule to include the flow resistance effect of vegetation on the hydrodynamics and thus also on the morphodynamics. The vegetation increases the bed roughness used in Eqs. (1) and (2), but not in the sediment transport rate formula to prevent increased sediment transport in vegetated grid cells. The bed roughness in the vegetated grid cells was computed using Baptist (2005). It was assumed that vegetation grows in each grid cell with a water depth smaller than an arbitrary 2 m, noting that we applied a constant discharge that is assumed to be the mean annual peak discharge. The mean discharge within a year would be much lower, thus with lower water levels. Every two days, the location of the vegetation was checked and adjusted if needed. Vegetation was removed if the water depth was larger than 2 m.

In Nays2D, the bank erosion computation is restricted to the outer banks, and based on an angle of repose and transverse sediment transport. When the angle of repose is exceeded, the volume of eroded bank material and the distance of bank line retreat are computed based on the cohesive sediment layer thickness. The curvilinear grid is then adjusted and smoothed. After adjustment of the bank lines, all grid cells are redistributed to maintain orthogonality and limit the range of grid cell sizes. The eroded cohesive bank material is deposited at the bank toe in a sub-grid operation, temporarily protecting the bank against erosion. In the following period, the deposited sediment is gradually eroded by transverse sediment transport, re-exposing the bank to bank erosion. In order to increase stability, a minimum channel width $W_{\min}$ was applied, with a default $W_{\min}$ of 100 m. In the sensitivity analysis, we determined the effect of the minimum channel width.

Bar–floodplain conversion in Nays2D depends on a threshold water depth. Here we used a threshold of 0.8 m as depth where vegetation settles. If the water depth in a grid cell is smaller than the threshold water depth, the grid cell is assumed to be vegetated and part of the banks. The vegetated area is then removed from the computational domain and the bank line is shifted accordingly.

In the IP-model, bank erosion is computed from the excess flow velocity near the eroding bank:

$$E = ku_b \tag{16}$$

where E is the bank line retreat (m/s), u_b is the excessive flow velocity near the eroding bank (m/s) and k is a erodibility coefficient commonly used as calibration parameter, here $k = 10^{-4}$. By definition, bar–

floodplain conversion in the inner bends is equal to the bank erosion rate of the opposite bank.

2.5. Model schematization and scenarios

The appropriate channel dimensions and boundary conditions for a single-threaded meandering channel were estimated using the empirical relations of (Kleinhans and Van den Berg, 2011). The conditions for the middle-scenario (D3D-A2) in Fig. 2 resulted in a single-threaded channel with alternate bars. Thus, these conditions were applied in our simulations.

Simplified boundary conditions were imposed in the simulations, for example constant discharge and uniform sediment, following Schuurman et al. (2013). The constant discharge was assumed to be the dominant or effective discharge. This means, in reality, that the discharge and water level would be lower during most of the year in reality. Preliminary model tests in braided rivers, using the same approach as for our Delft3D-simulations but with a yearly hydrograph, showed that the long-term statistics of bed topography are similar to a constant discharge. This justifies the use of a constant discharge.

To determine the effect of different kinds of inflow perturbations, we tested three perturbations: (1) no perturbation, (2) skewed inflow, (3) laterally migrating inflow (Fig. 3). In Delft3D, these perturbations were imposed in a channel with erodible banks and with non-erodible banks; in Nays2D and the IP-model the scenarios were only applied in a channel with erodible banks. In the Delft3D-simulations, we used an initial channel width of 200 m and a channel length of 20 km; In the Nays2D-simulations we used an initial channel width of 180 m and a channel length of 10 km; in the IP-model, we used a channel width of 200 m and a channel length of 100 km.

In the Delft3D simulations, a fixed rectangular computational grid with cell sizes of 50 × 20 m was applied. The simulations in Nays2D started with a rectangular grid with cell sizes of 50 × 20 m. During the meander simulation in Nays2D, bank erosion and bar–floodplain conversion adjusted the bank lines. Regridding was performed to keep the grid boundary fitted and to keep the transverse grid lines perpendicular to the channel centerline.

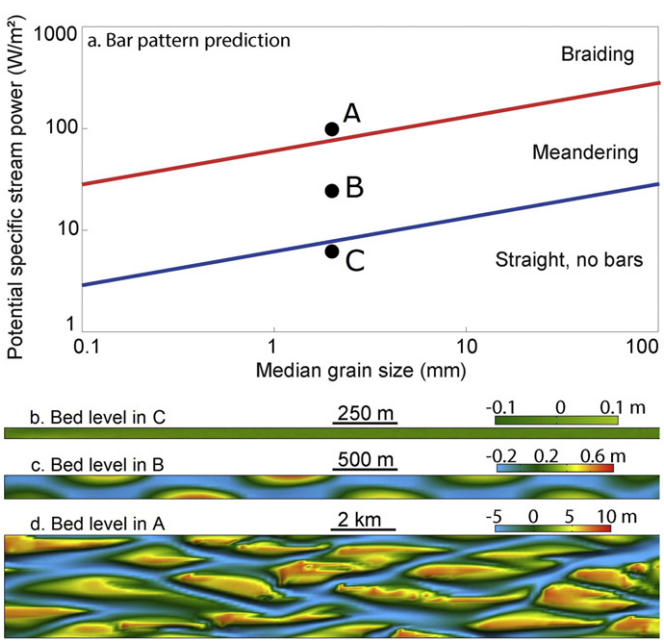

Fig. 2. a. Model scenarios for different bar patterns compared to the bar pattern predicted from the specific potential stream power (Kleinhans and Van den Berg, 2011); b. detrended bed level in run D3D-A1; c. detrended bed level in run D3D-A2; d. detrended bed level in run D3D-A3.

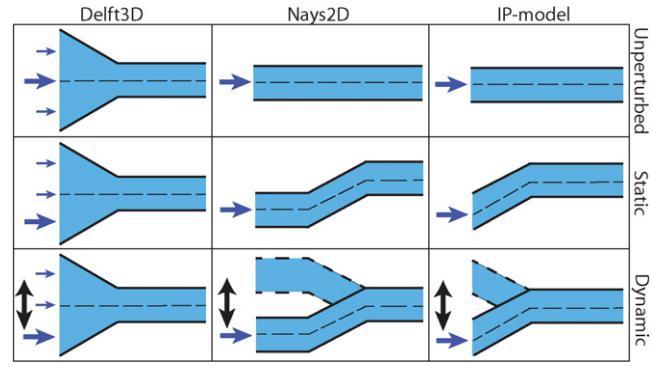

Fig. 3. Upstream inflow perturbation scenarios for Delft3D (left), Nays2D (middle) and the IP-model (right).

Although an extensive sensitivity analysis is out of the scope of this chapter, we determined the effect of spiral flow intensity on the meandering and morphology in Nays2D. For this, three values for N (Eq. (13)) were applied: 7 (adopted from Engelund, 1974), 11 (equal to Delft3D) and 13. For the bed roughness, a constant k_s of 0.15 m in Delft3D and a constant Manning's n of 0.028 in Nays2D were used. The default settings and model scenarios are given in Tables 2 and 3.

3. Analysis of model output

The analyses of the simulation results consisted of a combination of qualitative comparison between the bathymetries of different model runs and quantitative comparisons by using descriptive parameters for the meander shape. For the comparisons, the bathymetry was corrected for the initial downstream bed slope. For the Delft3D-results, the erodible, dry floodplains were removed from the bathymetries.

We quantified the meander pattern by three parameters: meander length, channel width, and sinuosity. Reach-averaged values of these parameters were recorded for each output timestep. For channel width, we used the width of the computational grid for Nays2D, and the distance between the outer banks for Delft3D. The sinuosity is the ratio between the initial channel length (10 km in Nays2D, 20 km in Delft3D and 100 km in the IP-model), and the length of the thalweg (Delft3D) or channel axis (Nays2D and the IP-model). The bar length was computed using a wavelet-analysis (Torrence and Compo, 1998) along the right bank (Delft3D) or as the double distance between adjacent inflection points (Nays2D and the IP-model).

3.1. Bar and meander lengths

We compared the meander length with an empirical relation of Dury (1976):

$$L_1 = 11W \tag{17}$$

where L_1 is meander length (m). For the initial channel width of 200 m, the predicted meander length L_1 is 2.2 km. We also compared the

Table 2
Default boundary conditions and initial settings.

Parameter	Delft3D	Nays2D	IP-model
Discharge Q (m^3/s)	2500	2500	2500
Initial width (m)	200	180	200
Initial depth (m)	6.8	6.8	6.8
Channel length (km)	20	10	100
Grain size D_{50} (mm)	2.0	2.0	2.0
Inflow migration period T (year)	23	1.4	10
Inflow migration amplitude (m)	300	300	500

Table 3
Model runs with specific conditions that deviate from the default settings (Table 2).

			Delft3D		Nays2D		IP model	
Inflow perturbation	Erodible outer banks	Bar-floodplain conversion	Run ID	Property	Run ID	Property	Run ID	Property
No	yes	*default*	D3D-A1	*default*	Nays-A1	*default*	IP-A1	*default*
Static	yes	*default*	D3D-A2	*default*	Nays-A2	*default*	IP-A2	*default*
Dynamic - slow	yes	*default*	D3D-A3	T = 46 year	Nays-A3	T = 2.8 year	-	-
Dynamic - medium	yes	*default*	D3D-A4	T = 23 year	Nays-A4	T = 1.4 year	IP-A3	T = 10 year
Dynamic - fast	yes	*default*	-	-	Nays-A5	T = 0.7 year	-	-
Static	yes	vegetation	D3D-B1	*default*	-	-	-	-
Dynamic - medium	yes	vegetation	D3D-B2	T = 23 year	-	-	-	-
Dynamic - medium (continuously)	yes	*default*	-	-	Nays-B1	restart month 8	-	-
Dynamic - medium (temporarily)	yes	*default*	-	-	Nays-B2	restart month 8	IP-B1	restart year 20
No	no	no	D3D-C1	*default*	-	-	-	-
Static	no	no	D3D-C2	*default*	-	-	-	-
Dynamic - medium	no	no	D3D-C3	T = 23 year	Nays-C1	T = 1.4 year	-	-

wavelength of the bars and meanders with bar lengths predicted by linear analysis for steady alternate bars (Crosato and Mosselman, 2009):

$$L_2 = 4\pi\lambda_w\left[(b+1)\frac{\lambda_w}{\lambda_s} - \left(\frac{\lambda_w}{\lambda_s}\right)^2 - \frac{(b-3)^2}{4}\right]^{-1/2} \tag{18}$$

where λ_s is the bed level adaptation length:

$$\lambda_s = \frac{h}{\pi^2}\left(\frac{W}{h}\right)^2\frac{1}{f(\theta)} \tag{19}$$

and λ_w is given in Eq. (6). For the initial stage, the predicted steady bar and meander length L_2 is 3.8 km. Furthermore, we compared the bar length of the free migrating bars with predictions by a linear analysis (Schielen et al., 1993):

$$L_3 = \frac{2W}{\sqrt{X}} \tag{20}$$

where X is iteratively determined from.

$$\varepsilon = \frac{-X(X+1)^3\delta}{\delta(X+1)(X+2)^2 - X(2X+1)} \tag{21}$$

and ε and δ are calculated with.

$$\varepsilon = \left[\frac{g}{C^2\pi}\frac{W}{h}\right]^2, \delta = \frac{g}{C^2(b-1)} \tag{22}$$

For the initial stage, the predicted free bar length L_3 is 830 m, thus several times smaller than the predicted steady bar and meander lengths. It should be noted, however, that the input parameters for the bar and length predictors vary in time and space, especially the channel width and water depth. Strictly, the predictors based on linear analyses (Eqs. (18) and (20)) are only valid for the initial stage, in which the bars have negligible height compared to the water depth. Furthermore, many more relations are available and they use the above merely to indicate the expected range of wavelengths.

3.2. Spatial damping of inflow perturbation

In flume experiments of Van Dijk et al. (2012) and Crosato et al. (2012), an inflow perturbation resulted in a steady alternate bar, either along the bank where the inflow migrates to or downstream of a groyne. Such steady bar could result in meander initiation. However, theory indicates that the effect of a flow perturbation on a meandering river bed behaves like an underdamped oscillator (e.g. Mosselman et al., 2006). Thus, the effect of an upstream perturbation would smoothly decay in downstream direction, which is visible by a decay of the amplitude of bars forced by the perturbation. We compared the decay of alternate bar amplitude downstream of the inflow perturbation in our simulations with predicted alternate bar amplitude decay (Struiksma et al., 1985):

$$z_{bs} = z_{b0}\exp\left[-\frac{s}{L_D}\right]\sin\left[\frac{2\pi}{L_2}(s+s_P)\right] \tag{23}$$

where z_{bs} is the near-bank bed level at downstream coordinate s (m), z_{b0} is the near-bank bed level at the upstream boundary (m), s_P is a spatial phase lag (m), and L_D is the damping length (m):

$$L_D = 2\lambda_w\left[\frac{\lambda_w}{\lambda_s} - \frac{b-3}{2}\right]^{-1} \tag{24}$$

We compared the decay in predicted height of the steady forced bars with the decay in bar height in the Delft3D simulations. Because flow curvature in a bend affects bar height and is not included in Eq. (23), we only compared the simulations with non-erodible banks. This way, we isolated the effect of the inflow perturbation on bar dimensions from the effect of meander bends. Eq. (23) is not valid for free migrating bars, as they do not experience a spatial nor temporal decay with constant and uniform conditions (Blondeaux and Seminara, 1985).

4. Results

This section starts by describing the modeling results of meander dynamics using different inflow perturbations in each of the models. Secondly, it goes into detail in the morphodynamic processes occurring

during meander initiation and expansion, and the reason why the upstream inflow perturbation affects meander behavior. Thirdly, we elaborate on the differences between the three models, employing the fact that each model has a specific way to model bank erosion, bend-cutoff and bar–floodplain conversion.

4.1. Meandering in Delft3D

4.1.1. Dynamic inflow

Dynamic inflow perturbation in combination with erodible banks in Delft3D resulted in a low-sinuosity meandering channel, started from a straight channel. The thalweg meandering was initiated by a steady bar directly downstream of the entrance and bank erosion at the opposite bank (Fig. 4a). As this bar grew and the bank erosion progressed, it triggered the formation of new bars further downstream, each with erosion at its opposite bank (Fig. 4b). After 20 to 30 years, the thalweg meandered over the entire length.

Modeled bank erosion rates were in the order of 16 m/year in the outer bends. The peak flow velocity and bank erosion rates occurred around 0.5–1 km downstream of the apex, causing downstream migration of the bars and incipient meander bends. The final bar height was around 3–4 m, with bar lengths of around 3–4 km and downstream migration rates of 0.4 km/year.

4.1.2. Effect of inflow perturbation

The effect of the upstream inflow perturbation on the bar and meander dynamics is shown in Fig. 5. Without inflow perturbation, bank erosion occurred along both sides of the channel, thus a symmetrically widening of the channel. At the same time, a mid-channel bar formed at the widest section. The channel widening expanded in downstream direction and induced more mid-channel bars further downstream. A static inflow perturbation resulted in erosion of the left bank directly downstream of the inflow, followed by the formation of a steady bar at around $x = 3$ km. The flow and sediment transport perturbations induced by this bar was sufficient to force the formation of more alternate bars further downstream, comparable to run D3D-A3 with migrating upstream inflow.

The lateral inflow migration rate affected the long-term evolution of the river in Delft3D. As shown in Fig. 6, a fast inlet migration, with a cycle period of 23 years, resulted in chute-cutoffs and mid-channel bars. This started with the most upstream alternate bar, disturbing the sinuous thalweg (Fig. 5A). A chute-cutoff of the most upstream alternate bar did not occur in case of a slower inlet migration with a period of 46 years.

Although the inflow perturbation affected the bar dynamics at the upstream 10 km significantly, the long-term difference between the model runs with different degrees of inflow perturbation was rather small. For example, the average channel width after full occupation of the channel by steady bars, was equal for the three runs with asymmetrical inflow (Fig. 5). Furthermore, the channel width continued to increase regardless of the upstream inflow, without a decline in widening rate. Thus, a dynamic equilibrium was not reached, independently of the inflow perturbation.

4.2. Meandering in Nays2D

4.2.1. Dynamic inflow

A dynamic inflow perturbation in Nays2D resulted in a persistently high-sinuosity meandering channel including neck-cutoffs (Fig. 7). Similar to the Delft3D-simulation, a non-migrating alternate bar formed directly downstream of the shifting entrance (Fig. 7a). The bar induced flow steering towards the opposite bank and thus local bank erosion. As the bars were non-migrating, the bank erosion resulted in an increasing channel bending. The most upstream bend forced the development of a non-migrating bar directly downstream, which triggered a second bend further downstream. This process continued until the entire reach was occupied by meander bends, after around 11 months.

The average meander length increased towards a steady length of around 2–3 km. This is in the same order of magnitude as the predicted meander length L_1 (2.2–2.7 km), but shorter than the predicted meander length L_2 (3.8 km) and shorter than the meanders in the low-sinuosity channels in Delft3D (around 3.5 km).

4.2.2. Effect of inflow perturbation

Without an inflow perturbation, the channel remained more or less straight (Fig. 8), with small high-mode bars developing at the upstream boundary and migrating in downstream direction. Further downstream, these high-mode bars evolved into alternate bars, but although some of these alternate bars became covered by vegetation and were removed from the computational domain, no meander bends were formed.

In case of a static inflow perturbation, high-sinuosity meander bends were formed: the upstream bend forced the formation of downstream bends. However, the sinuosity of the upstream bends gradually declined and bend amplitude decreased. This decrease in bend amplitude was partly caused by the smoothing procedure.

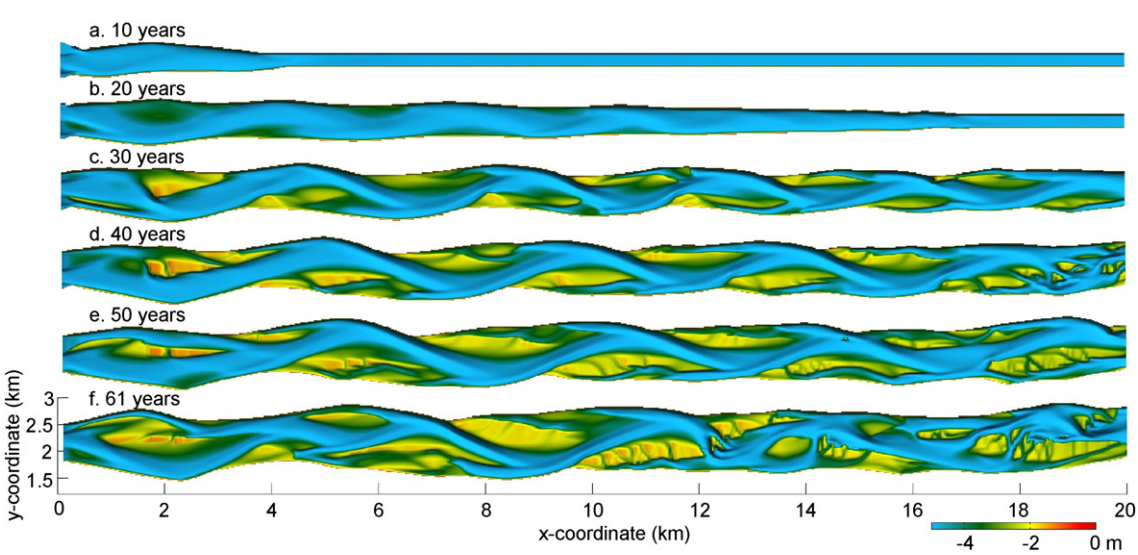

Fig. 4. Initiation and evolution of alternate bars and incipient meandering in run D3D-A3, with continuous upstream inflow migration and erodible banks. After around 40 years, mid-channel bars formed by chute-cutoffs.

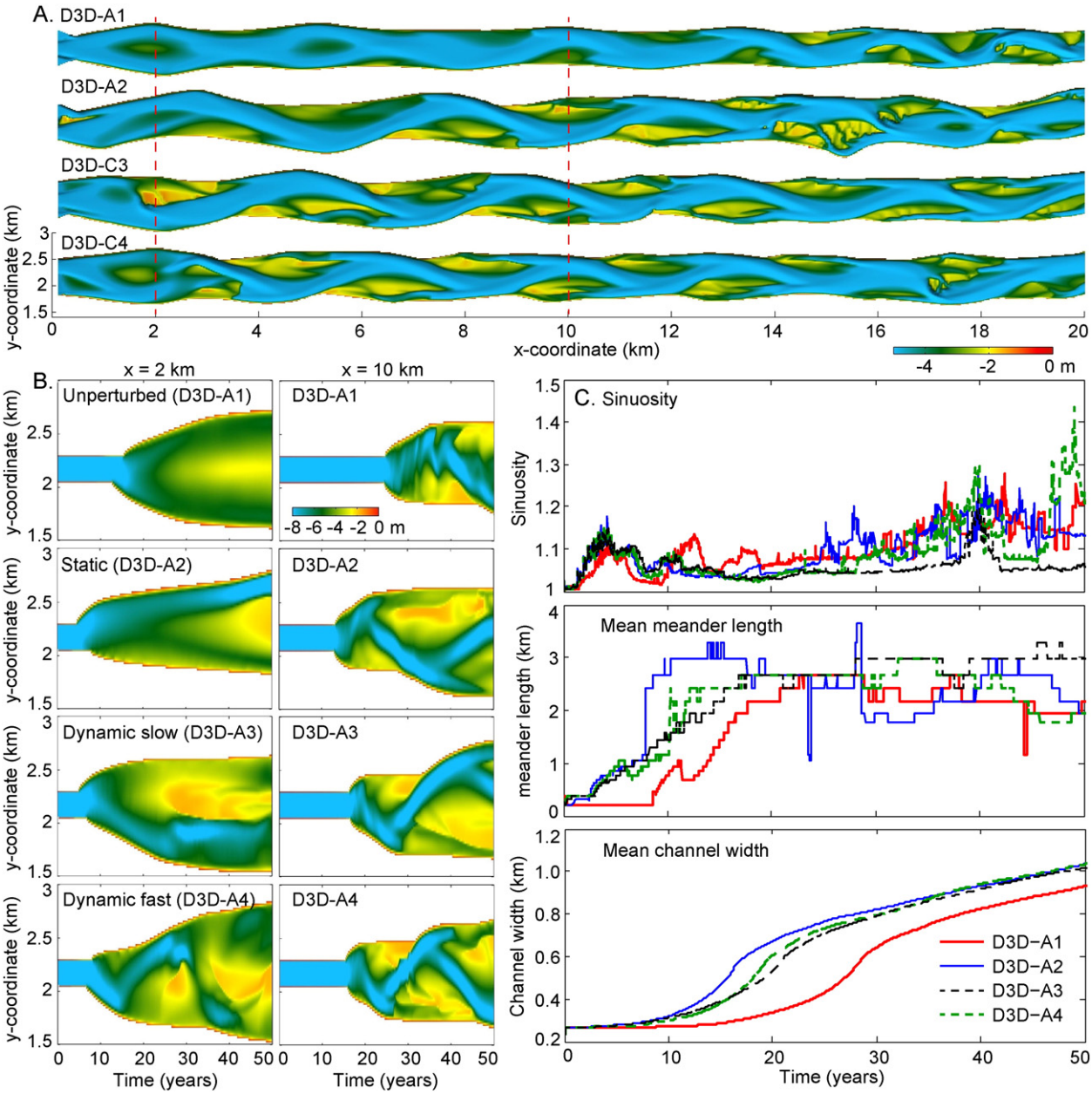

Fig. 5. Effect of inflow perturbations in Delft3D: A. Detrended bed level after 34 years; B. Time-space diagram of cross-sectional bed profiles at $x = 2$ km and $x = 10$ km; C. Channel statistics showing sinuosity, mean meander length and mean channel width.

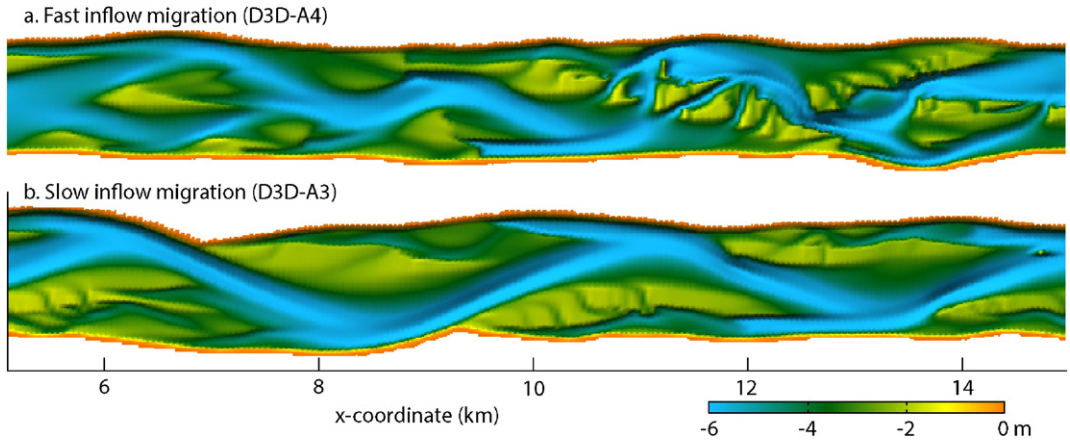

Fig. 6. Effect of the upstream inflow migration rate on the bar pattern in Delft3D after 55 years: chute-cutoffs and mid-channel bars in D3D-C3 (a) and alternate bars in D3D-C4 (b).

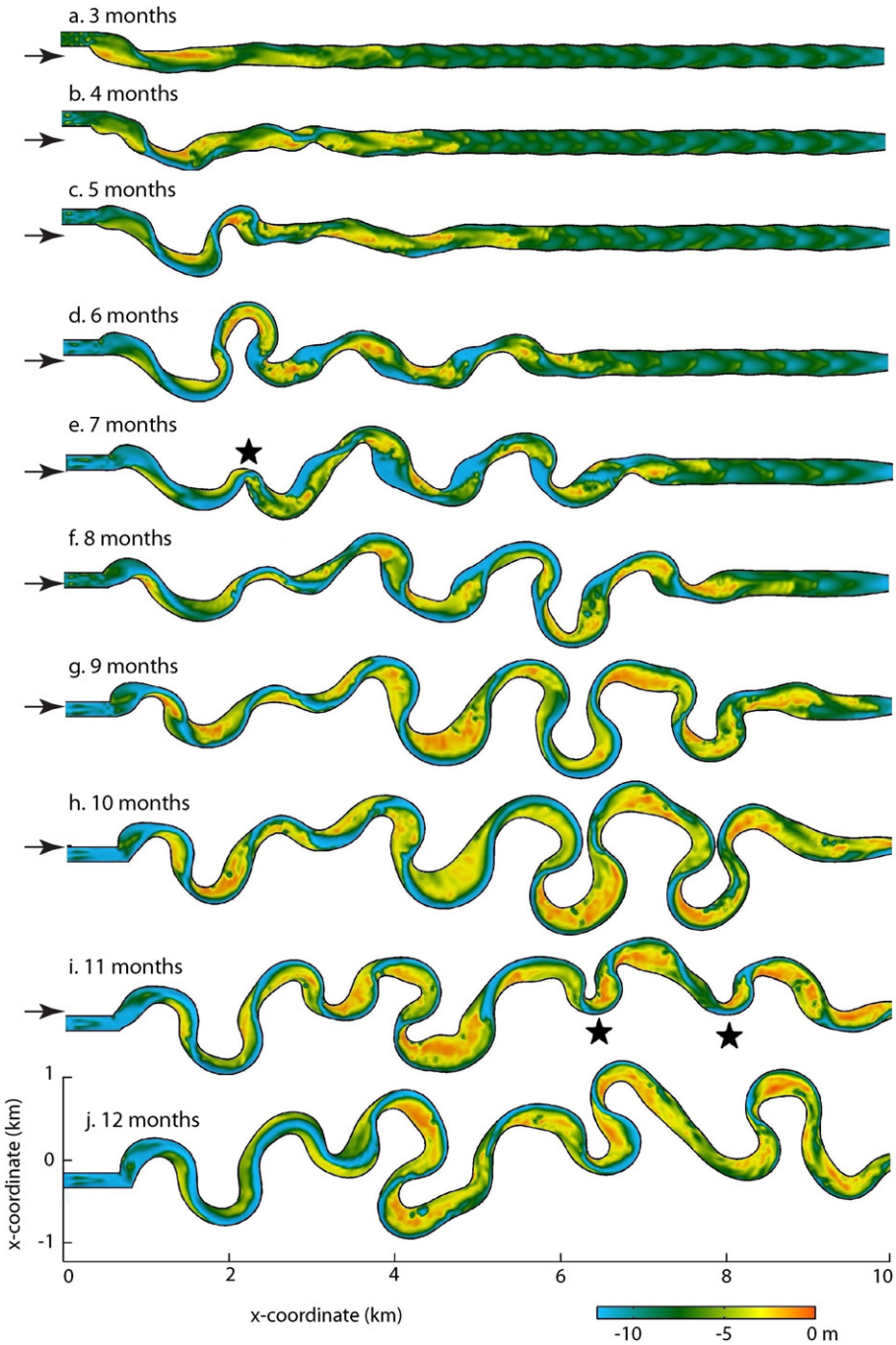

Fig. 7. Propagation of steady bars, bend initiation, bend expansion and neck-cutoffs in Nays2D (Run Nays-A4) with a continuously migrating upstream inflow. Stars denote a neck-cutoff, and black arrows denote $y = 0$ km.

Also, if the inflow dynamics were stopped after 8 months, the sinuosity of the upstream bends declined and the point bars in the upstream bends partly disappeared (Fig. 8C). Despite this, the overall statistics of the river hardly changed yet within the modeled period as the downstream bends continued to expand.

4.2.3. Sensitivity of meander dynamics

The inflow migration rate had a major effect on the meander dynamics in Nays2D (Fig. 8): meander migration and expansion rates were much lower in case of lower inflow migration rate. The strong increase in sinuosity and meander length occurred at a later stage in case of slower inflow migration: after around 5 months for a period of 0.7 years and after around 11 months for a period of 2.8 years.

The minimum allowed channel width and minimum allowed bed level only affected the meander pattern in Nays2D to a minor degree (Fig. 9). Nevertheless, the sinuosity and meander migration rates were slightly higher for a smaller minimum channel width and lower minimum bed level.

Fig. 9 shows that the meander pattern in Nays2D was also sensitive to parameter *N*. A higher spiral flow intensity resulted in a higher sinuosity, larger amplitude of the bends, smaller channel width and larger migration rates. A reason for the large sensitivity of the meanders to *N* is that the bank erosion rate is computed using the transverse sediment transport flux in the direction away from the eroding bank. In a meander bend, this transverse sediment transport is caused by the spiral flow.

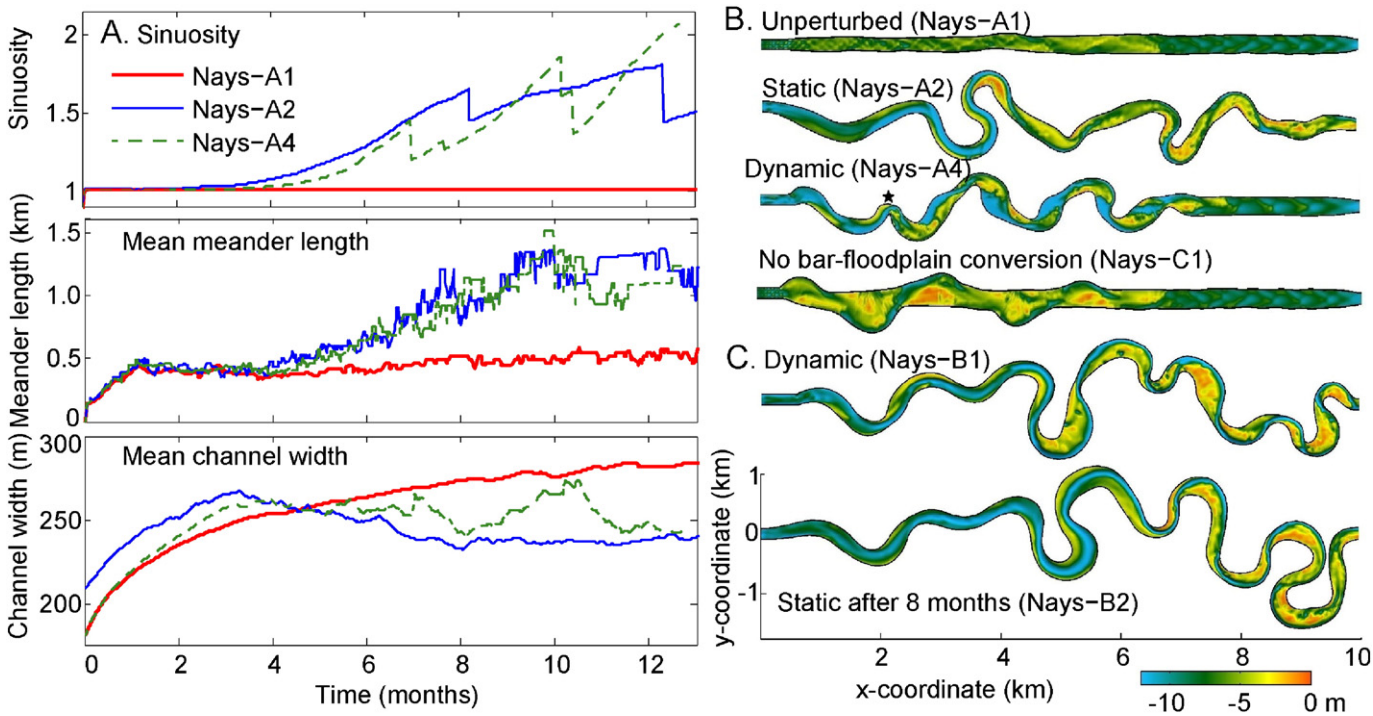

Fig. 8. Effect of inflow perturbations in Nays2D: A. Channel statistics; B. Bed levels after 7 months; C. Bed level after 16 months, thus 8 months after the switch from dynamic perturbation to static perturbation in Nays-B2. The star denotes a neck-cutoff.

4.3. Meandering in the IP-model

In the IP-model, high-sinuosity meanders developed in all of the scenarios with inflow perturbation (Fig. 10). In case of no inflow perturbation (not shown here), no bends formed at all, as meander migration in the IP-model is a function of channel curvature and its derivative (Eq. (4)). Interestingly, the difference in meander planform between a dynamic perturbation, a temporally dynamic perturbation and a static perturbation was relatively small. Although the channel shifted from right to left in case of a static perturbation, the sinuosity and meander lengths were similar. The sinuosities were in the order of 4 and meander length of 4–7 km, which is significantly larger than predicted by the empirical relations and observed in Delft3D and Nays2D. But when the initially regular meander bends became more complicated and diverse, the reach averaged meander length declined to around 4 km because of the development of compound meander bends.

4.4. Forced-free bar interactions

In the previous sections, we saw that channel curvature is the driving force for meandering in the IP-model, whereas inner bend bars are the drivers for meandering in Delft3D. Meandering in Nays2D is a combination of inner bend bars and channel curvature. Isolation of the effect of inflow perturbation on the bars, thus with fixed banks, is shown in Fig. 11. Without an inflow perturbation, overall deposition of around 10 cm occurred with superpositioned free migrating bars near the expanding deposition front. A perturbation, both static and dynamic, resulted in two large steady bars at the upstream, with heights of around 1 m for the most upstream bar and a bar length of around 5 km. The bar height rapidly declined in downstream direction, with the second alternate bar only a couple of cm's high (Fig. 11g). Thus, the bars showed a strong underdamped behavior. Indeed, the damping length L_D computed by Eq. (24) was 778 m, several times shorter than the steady bar length. This means that, for the applied conditions, the effect of a flow perturbation, both static and dynamic, on steady bars decays rapidly in downstream direction and only induces the formation of a few steady bars.

However, a dynamic inflow perturbation did affect the overall deposition and free migrating bars. Each time the cyclic migrating inflow reached its maximum range, a new deposition front formed, migrating in downstream direction with a celerity of around 3.3 km/year (Fig. 11e). And only with a dynamic inflow perturbation, free migrating bars continued to be formed, although with lower height than the free migrating bars formed in the first years (Fig. 11f).

When we take a closer look at the forced-free bars interaction in case we allow bank erosion (Run D3D-A4), we see again that free migrating bars formed in the first years (Fig. 12b). Also, expanding deposition fronts occurred. The deposition fronts were related to the initiation of new steady bars and had a celerity of around 5 km/year, which is in the same order of magnitude as predicted by kinematic wave celerity ($c = bq_s/h$). However, in contrast to (Fig. 11e), each steady bars initiated a new steady bar downstream, resulting in steady bars in the entire channel after almost 20 years (Fig. 12a). Although identified as steady bars, these bars migrated slowly in downstream direction with a celerity of around 0.3 km/year.

4.5. Modeling of bank erosion and bar–floodplain conversion

The difference in sinuosity between the different models is partly caused by the difference in bank erosion and bar–floodplain conversion methods. In Delft3D, bank erosion is directly related to local incision, which generally occurs when flow accelerates in the outer bend and thus increases local sediment transport. However, the flow in the Delft3D simulations caused translation of the incipient meanders rather than expansion; the bars mainly migrated downstream instead of expanding in lateral direction. This suggests that the flow adaptation length in Delft3D was large compared to the bar length, or that the spiral flow was too weak compared to the gravity-induced bed slope effect to build sufficiently high point bars for high sinuosity meandering.

In Nays2D, the bank erosion rate is a function of the transverse sediment transport driven by spiral flow that removes the failed bank

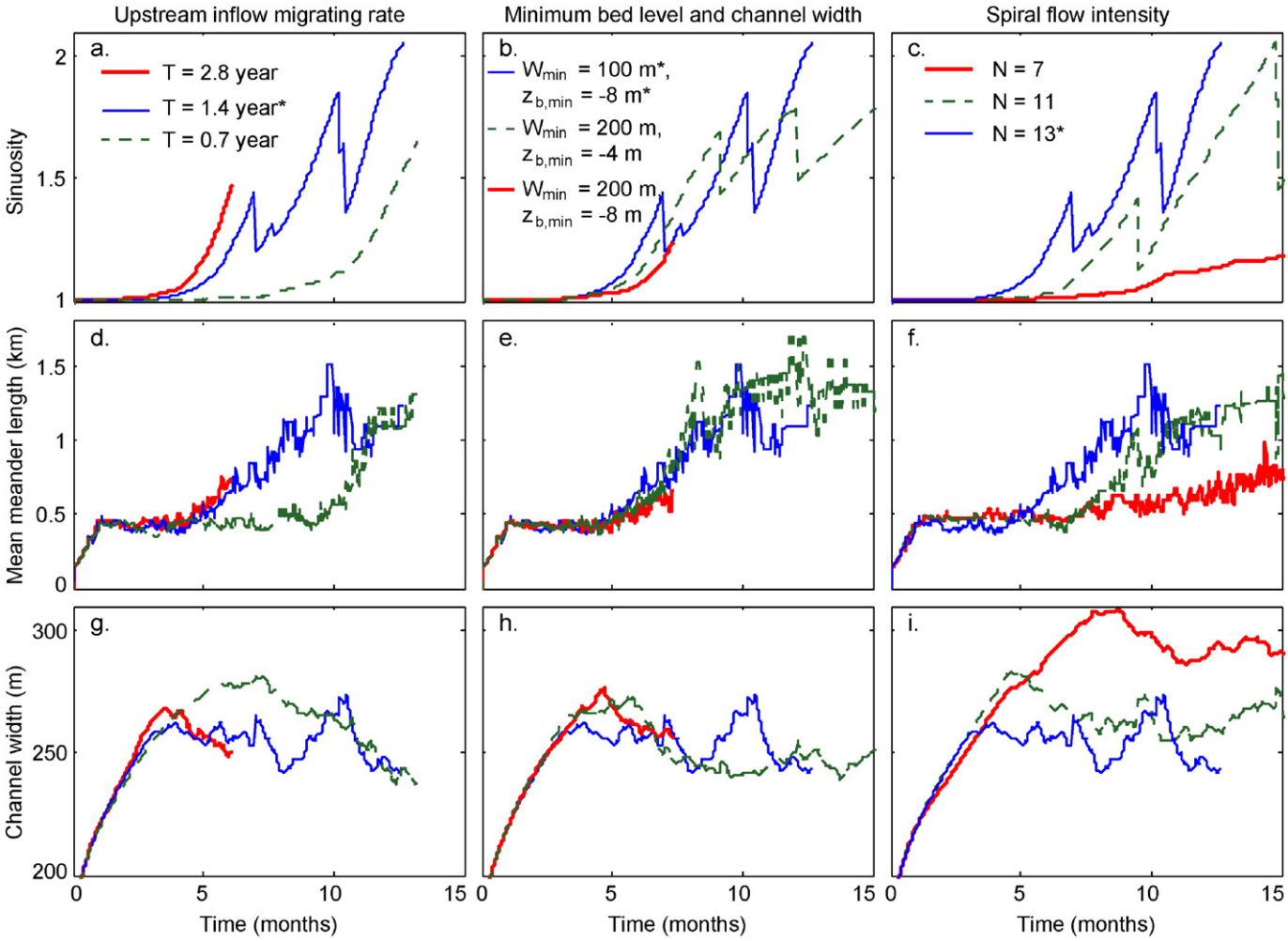

Fig. 9. Sensitivity of sinuosity (a–c), mean meander length (d–f) and channel width (g–i) in Nays2D on inflow migration rate (a, d, g); minimum channel width and bed level (b, e, h); and spiral flow intensity (c, f, i). * denotes default settings.

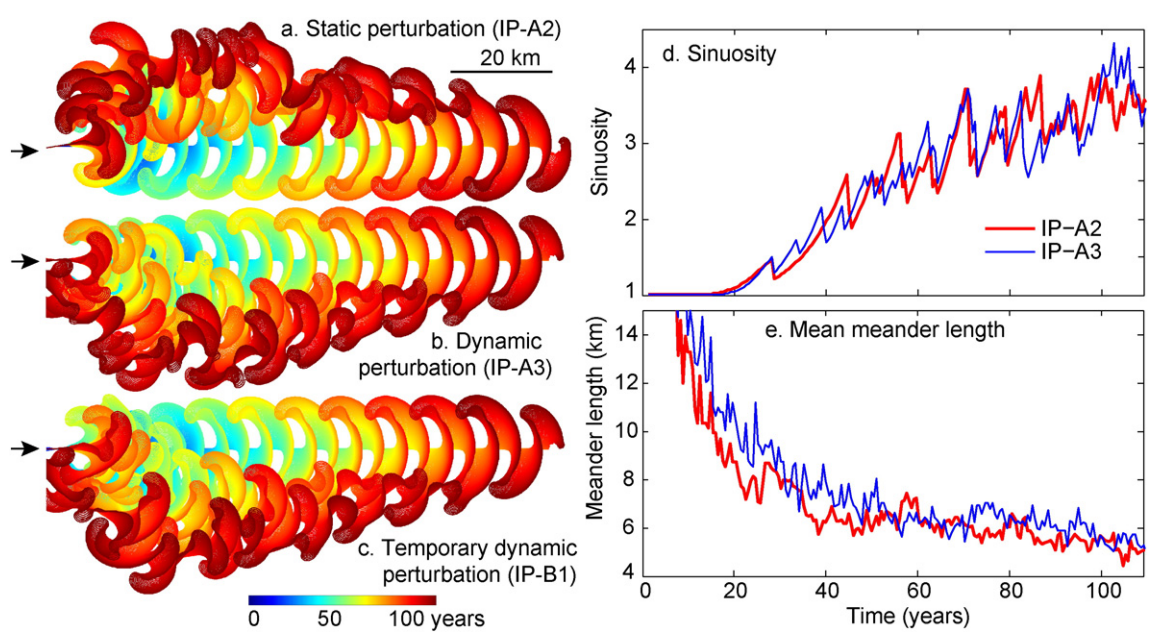

Fig. 10. Effect of inflow perturbations on meander migration in the IP-model: a. to c. Timeseries of channel centrelines, with flow from left to right and colors indicating age from blue to red; d. sinuosity and e. meander length, both showing no effect of the inflow perturbation.

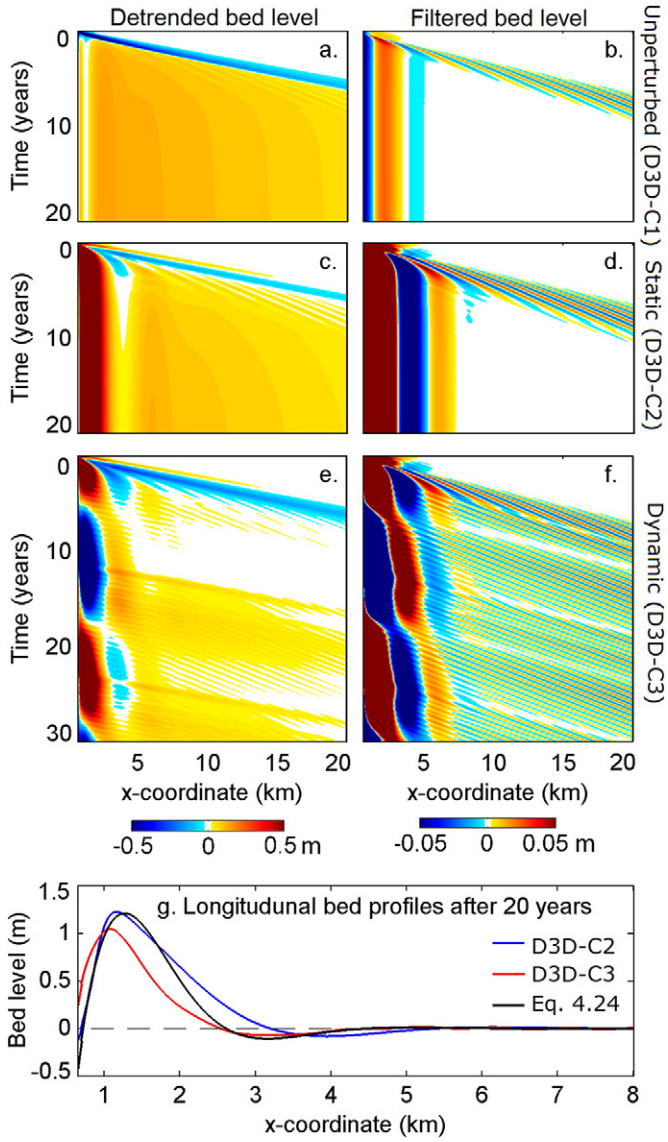

Fig. 11. Time-space diagrams of bed level evolution in the Delft3D-simulations with fixed banks and different inflow perturbations. In [a, b, c], the detrended bed levels of a profile along the right bank are given. In [b, d, f], the filtered bed levels, defined as the bed levels detrended by initial bed level minus the cross-sectional average bed levels to remove the large-scale deposition and erosion, are given. g. shows two longitudinal profiles made by the model and predicted by Eq. (23) after 20 years.

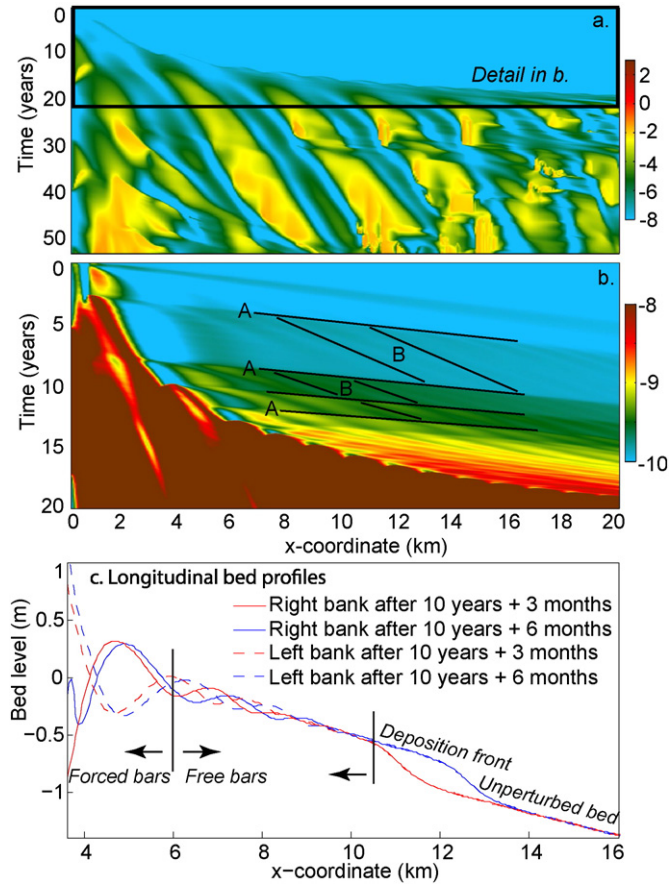

Fig. 12. a. Time-space diagram of a longitudinal profile along the right bank in run D3D-A4, with large nearly steady forced bars; b. detail of the migrating free bars before presence of the large steady bars and deposition front; c. longitudinal non-detrended bed profiles at two time steps, showing from upstream to downstream: forced bars, free migrating bars, deposition front and unperturbed bed. The black lines over the steady bars in a. have a slope of 130 m/year; lines A in b. have a slope of 1.3 km/year; lines B in b. have a slope of 8 km/year.

material. The spiral flow intensity was larger than in Delft3D due to the larger channel curvature. This caused larger bank erosion rates and further increase of flow curvature and spiral flow intensity. Furthermore, it resulted in more pronounced point bars and deeper outer bends, which can be seen for example along the bar edges: compare the smooth transition along the Delft3D-bars (Fig. 13a) with the Nays2D-bars (Fig. 13b).

Bar–floodplain conversion in Nays2D also differs from Delft3D, as Delft3D has basically no bar–floodplain conversion mechanism. If we turn off the bar–floodplain conversion in Nays2D, the meander morphology differed significantly from the case with bar–floodplain conversion: a low-sinuosity meandering channel formed instead of the usual high-sinuosity meanders (Fig. 8). The meander initiation process was similar, but meander expansion rates and maximum meander amplitude were much smaller in case of no bar–floodplain conversion. Furthermore, the inner bend bars were relatively irregular, especially at $x = 2$ km and $x = 4$ km. Thus, the inner bend bars formed in case of no bar–floodplain conversion differed from the smooth inner bends in case of bar–floodplain conversion.

In Delft3D, inner bend deposition mainly occurred at the lee of the bars in scroll-bar type bar-tail limbs, with the bar only at the upstream being connected to the banks and a bed level depression between the bar-tail limb and the bank (Fig. 13a). This particular bar shape was similar to the example of Fig. 1f, and had implications for bar–floodplain conversion and chute-cutoffs: the bed level depression complicated bar–floodplain conversion, and chute-cutoffs occurred frequently as the connections between bars and floodplain were relatively short.

The asymmetrical shape of the steady bars with bar-tail limbs had also implications for the effect of vegetation on the bar morphology (Fig. 13c, d): the vegetation patches on the bars were narrow and tall, directing diagonal in downstream direction towards the river axis. Also, the connections between the floodplain and the vegetated patches were relatively short. Whether this typical vegetation pattern is the cause or consequence, the vegetated bars had the same typical shape as the vegetation patches. Anyway, due to the short connection between the bars and floodplain, the vegetation did not promote the development or lateral expansion of a point bar like in the examples of Fig. 1b and c, although the flow velocity over the bars decreased by around 2/3. A reason for this is that the highest flow velocity in the channel is located at the inflection points instead of at the bend apexes. Thus, addition of vegetation in Delft3D did not result in high-sinuosity meandering, and had a smaller effect than the bar–floodplain conversion mechanism in Nays2D.

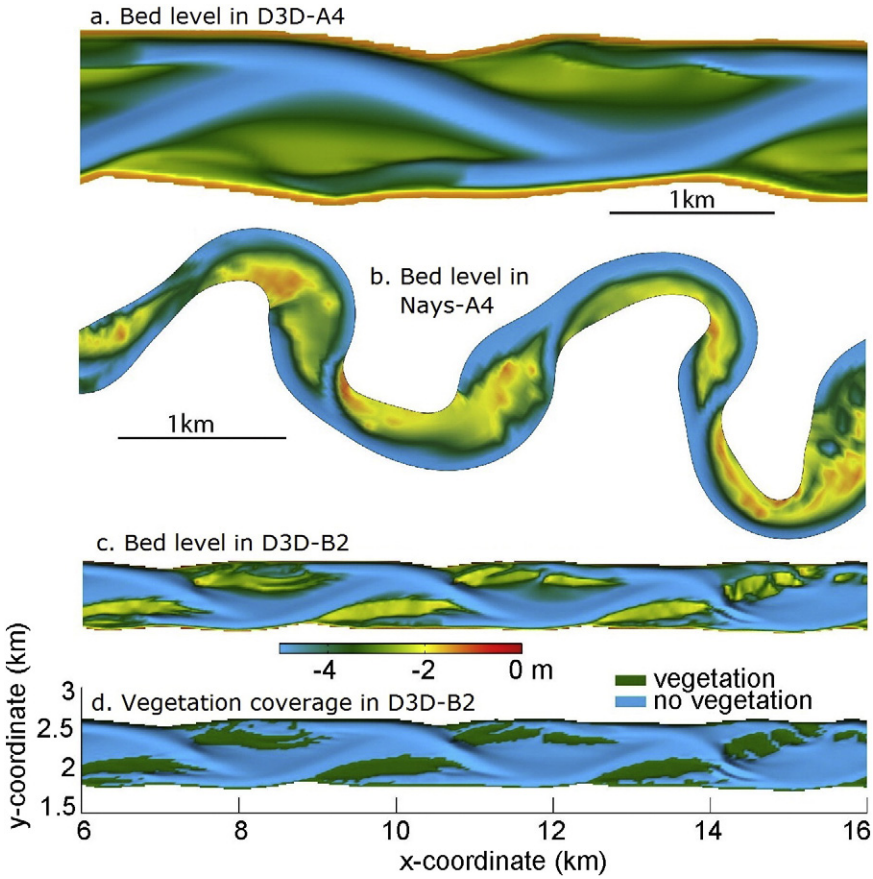

Fig. 13. Asymmetrical shape of alternate bars in a. Delft3D and b. Nays2D. Note the similarity in bar shape between (a) and Fig. 1f. c. Detrended bed level in run D3D-B2 after 34 years; d. vegetation coverage in run D3D-B2 after 34 years.

5. Discussion

We studied the initiation and development of river meandering in response to upstream channel curvature perturbations and floodplain formation, employing the differences between three numerical models: the classical IP-model and two state-of-the-art models. We first discuss the interactions between bends, forced bars and free bars in different river evolution stages and sinuosities in view of the well-known hypothesis that forced alternate bars initiate meandering. Second, we discuss the effects of upstream inflow perturbation on meander initiation and dynamics, and evaluate the hypothesis that upstream inflow perturbation is a necessary condition for meandering. Third, we discuss the effects of the assumptions behind bar–floodplain conversion methods on the meandering dynamics and cutoff style, in view of the hypothesis that meandering requires a dynamic balance between bank erosion and self-forming floodplain. Fourth, we discuss the capability and applicability of the models and propose future research topics.

5.1. Meander initiation: free bars, forced bars and bends

This study showed that meander initiation in a straight channel is the result of a downstream propagating sequence of (1) a steady alternate bar, followed by (2) local bank erosion along the opposite bank, (3) increased thalweg curvature and flow asymmetry, and (4) onset of a new steady alternate bar further downstream. Only in case of channel curvature, the flow asymmetry suffices for the onset of steady alternate bars downstream of a perturbation. The incapacity of a bed level perturbation alone to cause bar development further downstream in a straight channel is in agreement with theory of Struiksma et al. (1985) that predicts bar damping in channels with low width-depth ratio. Therefore, in the damped regime, bends are required for downstream propagation of a perturbation, by means of flow redistribution and localized bank erosion, resulting in a meandering channel.

If a steady alternate bar is absent, sufficient reach length also suffices for the formation of alternate steady bars and incipient meandering, even when mid-channel bars are located upstream (run D3D-A1, see Fig. 5A). Likewise, the mid-channel bar formed by a chute-cutoff in run D3D-A4, hardly affected the alternate bars and incipient meandering process further downstream. However, our simulations did not show a gradual downstream increase in meander amplitude, which would be expected if meanders indeed amplify in downstream direction. The specific interaction between bars and bends during the initiation of meandering implies that the IP-type meander migration models that use channel curvature and assume perfect match between bars and bends, are invalid for initiation of meandering.

The model results confirmed that free migrating bars, such as in the examples of Fig. 1 have little to no impact on meander initiation and dynamics. Surprisingly, the free migrating bars were affected by inflow dynamics: they only continued to form in case of a dynamic inflow perturbation. Even without suppression by steady alternate bars as described by Crosato et al. (2012), free bars were only present in the initial stage or in case of a dynamic inflow perturbation (Fig. 11). This suggests that free migrating bars, at least in the numerical models, require a large perturbation and are not purely the result of an intrinsic instability as was suggested by e.g. Seminara and Tubino (1989) and Tubino and Seminara (1990).

5.2. Necessity of inflow perturbation dynamics for sustained meandering

Flume experiments of Van Dijk et al. (2012) and linear models (Lanzoni and Seminara, 2006) suggested that a dynamic inflow perturbation - mimicking the presence of a migrating upstream

meander bend - is a necessary boundary condition for sustained meander dynamics. However, the results from both Nays2D and Delft3D demonstrated that perturbation dynamics alone is not sufficient for high-sinuosity meanders. Our model results showed that, although the upstream river reach, thus close to the perturbation, was strongly affected by the perturbation dynamics, the overall additional effect of perturbation dynamics was relatively small compared to a static perturbation. Moreover, in Delft3D, the inflow perturbation had hardly an effect at all on the morphology (Fig. 5). An explanation for this is that an inflow perturbation only affects the bed over a length of around one to two bar lengths downstream of the perturbation, as we saw in the Delft3D-simulation with fixed channel boundaries (Fig. 11). Here, the damping length of the steady bars was less than one bar length, thus the height of the bars induced by the inflow perturbation declined rapidly in downstream direction, in agreement with theory (e.g. Struiksma et al., 1985).

However, upstream channel dynamics in Nays2D significantly affected the high-sinuosity meander pattern and dynamics within the entire reach. This demonstrates again, like the propagating cycle of meander initiation, that the effect of a (steady) bar rapidly fades in downstream direction, whereas the effect of a meander bend propagates in downstream direction.

5.3. Necessity of bar–floodplain conversion for sustained meandering

The key to high-sinuosity meandering was found to be, besides well-known basic conditions for meandering such as appropriate width-depth ratio, grain size and bank erosion, the combination of a channel curvature perturbation and bar–floodplain conversion. Evidence for this was the difference between the meandering in Delft3D on one hand, and the meandering in Nays2D and the IP-model on the other hand. The meandering in Delft3D remained low-sinuous in the runs without explicit bar–floodplain conversion. In contrast, with the bar–floodplain conversion in Nays2D and the IP-model, high-sinuosity meanders developed. Thus, bars alone (the bar push) and bank erosion (bank pull) were found to cause insufficient redirection of flow away from the inner bend and towards the outer bend, described by e.g. Dietrich and Smith (1984), to induce high-sinuosity meandering. Addition of something like 'inner bank push', which represents the conversion of inner-bend bars into floodplain, was necessary for high-sinuosity meandering. This has been demonstrated before by Van Dijk et al. (2012) and Van Dijk et al. (2013b) in their flume experiments.

The bar–floodplain conversion is an important link in the morphodynamic cycle of river meandering (Fig. 14): the formation of alternate bars and pointbars, conversion of these bars into floodplain, and conversion of floodplain into channel by bank erosion. Each of these processes is found to be important for high-sinuosity meandering. The underlying process of the bar–floodplain conversion is, for example, vegetation encroachment and entrapment of sediment between the vegetation (Rominger et al., 2010). Furthermore, Constantine et al. (2014) suggested that an increase in river sediment transport accelerates inner bar aggradation, and thus stimulates bar–floodplain conversion and meander dynamics. The leading role of bar–floodplain conversion, however, differs from the findings of Hooke (2007), Gautier et al. (2010), Eke (2013) and Van de Lageweg et al. (2014) that outer bend bank erosion is the leading process and is followed by bar growth and bar–floodplain conversion. Sinuosity and specific conditions may explain this contradiction, for example easy-erodible outer banks diminish the need for flow concentration along the outer bank to erode the outer bank, and thus the necessity of the inner bank push. Regardless of the leading process, if bar–floodplain conversion follows bank erosion at a decent pace, an important ingredient for high-sinuosity meandering is present.

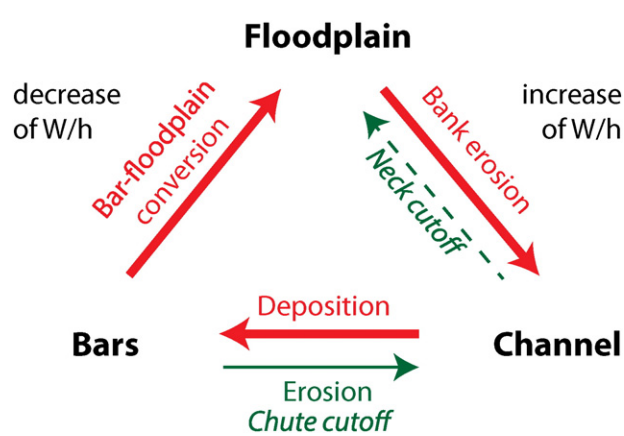

Fig. 14. Morphodynamic cycle in meandering rivers. Arrows indicate positive feedbacks, with dominant processes indicated by bold arrows and minor processes by narrow arrows.

The balance between bank erosion and bar–floodplain conversion rates is hard-coded in the IP-type models, and emerge in Nays2D in the current study and in Asahi et al. (2013). Alternatively or complementary, reduction of bank erosion rates, for example by temporal bank protection by failed bank material (Engel and Rhoads, 2012), give the inner bend time to develop and to keep pace with the bank erosion (Parker et al., 2011; Eke et al., 2014). However, the assumption that the inner bend bar shape mirrors the shape of the channel banks should be applied with care. A reason for this are the complicated shapes of the bars in low-sinuosity meanders. The typical shape of alternate bars in low-sinuosity channels contributes to the occurrence of chute-cutoffs. In line with earlier studies (Tal and Paola, 2010; Van Dijk et al., 2013a), our Delft3D simulations demonstrated that channel widening followed by chute-cutoffs precludes high-sinuosity meandering. Thus, besides redirection of the flow to the outer bank, prevention of chute-cutoffs is essential. This, again, advocates for the addition of inner bank push, as bars are more susceptible to chute-cutoffs than floodplain.

Furthermore, the Delft3D simulations showed that coupling of bar growth, vegetation encroachment and bar–floodplain conversion in a low-sinuosity channel does not lead to simple textbook pointbars with periodic scrolls that mirror the outer bank shape. Furthermore, vegetation creates its own complicated patterns, as also demonstrated in the flume experiments of Van Dijk et al. (2013a). This is important for the overall pattern, because Schuurman and Kleinhans (2015) demonstrated that the bar-tail limbs have a large influence on channel dynamics, which may be similar to the effects of the bar-tail type structures found in low-sinuosity meander bends (Fig. 1f). More understanding is needed about the effect of complicated inner bend bar shape on meander migration.

5.4. Progress in meander dynamics modeling

Combined strengths and weaknesses of the two state-of-the-art models show where progress can be made. To begin with, it is clear from this study that at least two-dimensional modeling is required to capture the natural dynamics of meandering rivers, with both accounting for channel dynamics and bar dynamics. The simplified symmetrical profiles applied in many meander migration models neglects independent dynamics of bars and bends. Many multi-dimensional physics-based models simulate the hydrodynamics, sediment transport and bed level change required for meandering. However, one step further, which is the coupling with bank erosion, is more challenging as it includes a new set of processes and parameters such as bank stability, bank failure and cohesiveness of the banks.

Even more important, our study demonstrated that this floodplain to channel conversion is insufficient for meandering and the models need to go, at least, one more step further: accounting for bar–floodplain conversion. This step is still in its infancy and not included yet in any physics-based model applied in the practice of river engineering,

which hampers the application of these models for dynamically meandering rivers. This is reflected by the extremely high migration rates in our Nays2D-simulations, with high-sinuosity reached within a year. An explanation is the difference between timescales of bar dynamics, vegetation growth and bank erosion, which complicates their interactions. Part of this, is the inter-annual, seasonal, variation in vegetation growth and discharge, which is a challenge to include in meander migration models. For example, the method used in Nays2D for converting bars into floodplain was found to be overly effective, which led to formation of a high-sinuosity channel within a year. The differences in timescales also argue for carefulness in comparing model results with flume experiments.

Clearly, modeling of bar–floodplain conversion and the underlying processes requires further research. Realistic vegetation growth and dispersion rules, and addition of cohesive sediment, with deposition of fines expected in the lee of the bars and on the higher bars, could improve meander migration modeling. Following Corenblit et al. (2009), vegetation succession and transverse gradients in vegetation types should be part of these improvements. Obviously, this also requires improvement of the feedback from vegetation to the hydrodynamics, sediment transport and bank stability. Another item that could enhance meander modeling is preservation of floodplain deposits and relict channels, following Motta et al. (2012). Thus, the challenge is addition of the relevant processes in a reductionist approach in state-of-the-art meander migration models, which will help us to fully understand meander migration for a wide range of conditions.

6. Conclusions

Based on the study of meander migration in three numerical morphodynamic models with different parameterizations for floodplain formation and destruction, we conclude the following:

1. Initiation of meandering requires either an upstream forcing or sufficient reach length for the onset of a steady bar that results in incipient meandering. Free migrating bars cause insufficient flow perturbation to form meanders.
2. Modeling of meander migration requires the simulation of both bar morphodynamics and channel bank dynamics, especially in low-sinuosity meandering rivers, in which bar morphology is less related to bend morphology (in high-sinuosity rivers, the bars and channels are more correlated as bars are forced by channel curvature).
3. A dynamic inflow perturbation significantly enhances meander development and induces a high-sinuosity channel, but hardly affects low-sinuosity meandering.
4. Bar–floodplain conversion, or 'inner bank push', is required for the development of high-sinuosity meanders; bars alone are insufficient. A fast floodplain conversion parameterization of this complicated process results in high-sinuosity meandering with neck-cutoffs. In contrast, simplified simulation of vegetation encroachment allows frequent chute-cutoffs to limit the sinuosity

Acknowledgments

MGK and FS are supported by the Netherlands Organisation for Scientific Research (NWO) (grant ALW-Vidi-864-08-007 to MGK). We thank Hans Middelkoop, Gary Parker, Wout van Dijk, Wietse van de Lageweg and Alessandra Crosato for discussions. Deltares and Royal HaskoningDHV are acknowledged for collaboration.

References

Asahi, K., Shimizu, Y., Nelson, J., Parker, G., 2013. Numerical simulation of river meandering with self-evolving banks. J. Geophys. Res. 118, 2208–2229. http://dx.doi.org/10.1002/jgrf.20150.

Baptist, M.J., 2005. Modelling Floodplain Biogeomorphology. Technical University Delft, Delft, The Netherlands.

Blondeaux, P., Seminara, G., 1985. A unified bar bend theory of river meanders. J. Fluid Mech. 157, 449–470. http://dx.doi.org/10.1017/S0022112085002440.

Camporeale, C., Perucca, E., Ridolfi, L., 2008. Significance of cutoff in meandering river dynamics. J. Geophys. Res. 113, F01001. http://dx.doi.org/10.1029/2006JF000694.

Constantine, J.A., Dunne, T., Ahmed, J., Legleiter, C., Lazarus, E.D., 2014. Sediment supply as a driver of river meandering and floodplain evolution in the Amazon Basin. Nat. Geosci. 7, 899–903. http://dx.doi.org/10.1038/ngeo2282.

Constantine, J.A., McLean, S.R., Dunne, T., 2010. A mechanism of chute cutoff along large meandering rivers with uniform topography. Geol. Soc. Am. Bull. 122, 855–869. http://dx.doi.org/10.1130/B26560.1.

Corenblit, D., Steiger, J., Gurnell, A.M., Tabacchi, E., Roques, L., 2009. Control of sediment dynamics by vegetation as a key function driving biogeomorphic succession within fluvial corridors. Earth Surf. Process. Landf. 34, 1790–1810. http://dx.doi.org/10.1002/esp.1876.

Crosato, A., 1987. Simulation model of meandering processes of rivers. Int. Conf. Euromech 215: Mechanics of Sediment Transport in Fluvial and Marina Environments, Extended Abstracts. University of Genova, Genova, Italy, pp. 158–163.

Crosato, A., Mosselman, E., 2009. Simple physics-based predictor for the number of river bars and the transition between meandering and braiding. Water Resour. Res. 45, W03424. http://dx.doi.org/10.1029/2008WR007242.

Crosato, A., Saleh, M.S., 2010. Numerical study on the effects of floodplain vegetation on river planform style. Earth Surf. Process. Landf. 36, 711–720. http://dx.doi.org/10.1002/esp.2088.

Crosato, A., Desta, F.B., Cornelisse, J., Schuurman, F., Uijttewaal, W.S.J., 2012. Experimental and numerical findings on the long-term evolution of migrating alternate bars in alluvial channels. Water Resour. Res. 48, W06524. http://dx.doi.org/10.1029/2011WR011320.

Crosato, A., Mosselman, E., Desta, F.B., Uijttewaal, W.S.J., 2011. Experimental and numerical evidence for intrinsic nonmigrating bars in alluvial channels. Water Resour. Res. 47, W03511. http://dx.doi.org/10.1029/2010WR009714.

Deltares, 2009. Delft3D-FLOW User Manual, Simulation of Multi-dimensional Hydrodynamic Flows and Transport Phenomena, Including Sediments. Deltares, Delft, The Netherlands.

Dietrich, W.E., Smith, J.D., 1984. Influence of the point bar on flow through curved channels. Water Resour. Res. 19, 1173–1192. http://dx.doi.org/10.1029/WR019i005p01173.

Duan, J.G., Julien, P.Y., 2005. Numerical simulation of the inception of channel meandering. Earth Surf. Process. Landf. 30, 1093–1110. http://dx.doi.org/10.1002/esp.1264.

Duan, J.G., Julien, P.Y., 2010. Numerical simulation of meandering evolution. J. Hydrol. 391, 34–46. http://dx.doi.org/10.1016/j.jhydrol.2010.07.005.

Dulal, K.P., Kobayashi, K., Shimizu, Y., Parker, G., 2010. Numerical computation of free meandering channels with the application of slump blocks on the outer bends. J. Hydro Environ. Res. 3, 239–246. http://dx.doi.org/10.1016/j.jher.2009.10.012.

Dury, G.H., 1976. Discharge prediction, present and former, from channel dimensions. J. Hydrol. 30, 219–245. http://dx.doi.org/10.1016/0022-1694(76)90102-5.

Edwards, B.F., Smith, D.H., 2002. River meandering dynamics. Phys. Rev. E 65, 046303. http://dx.doi.org/10.1103/PhysRevE.65.046303.

Eke, E., 2013. Numerical modeling of river migration incorporating erosional and depositional bank processes. University of Illinois, Illinois, United States.

Eke, E., Parker, G., Shimizu, Y., 2014. Numerical modeling of erosional and depositional bank processes in migrating river bends with self-formed width: morphodynamics of bar push and bank pull. J. Geophys. Res. 119, 1455–1483. http://dx.doi.org/10.1002/2013JF003020.

Engel, F.L., Rhoads, B.L., 2012. Interaction among mean flow, turbulence, bed morphology, bank failures and channel planform in an evolving compound meander loop. Geomorphology 163-164, 70–83. http://dx.doi.org/10.1016/j.geomorph.2011.05.026.

Engelund, F., 1974. Flow and bed topography in channel bends. Hydraul. Div. Am. Soc. Civ. Eng. 100, 1631–1648.

Engelund, F., Hansen, E., 1967. A Monograph on Sediment Transport in Alluvial Streams. Da. Tech. Press, Copenhagen, Denmark.

Engelund, F., Skovgaard, O., 1973. On the origin of meandering and braiding in alluvial streams. J. Fluid Mech. 57, 280–302. http://dx.doi.org/10.1017/S0022112073001163.

Erskine, W., Chalmers, A., Keene, A., Cheetham, M., Bush, R., 2009. Role of a rheophyte in bench development on a sand-bed river in southeast Australia. Earth Surf. Process. Landf. 34, 941–953. http://dx.doi.org/10.1002/esp.1778.

Erskine, W., Keene, A., Bush, R., Cheetham, M., Chalmers, A., 2011. Influence of riparian vegetation on channel widening and subsequent contraction on a sand-bed stream since European settlement: Widden Brook, Australia. Geomorphology 147-148, 102–114. http://dx.doi.org/10.1016/j.geomorph.2011.07.030.

Fredsoe, J., 1978. Meandering and braiding of rivers. J. Fluid Mech. 84, 609–624. http://dx.doi.org/10.1017/S0022112078000373.

Gautier, E., Brunstein, D., Vauchel, P., Jouanneau, J., Roulet, M., Garcia, C., Guyot, J., Castro, M., 2010. Channel and floodplain sediment dynamics in a reach of the tropical meandering Rio Beni (Bolivian Amazonia). Earth Surf. Process. Landf. 35, 1838–1853. http://dx.doi.org/10.1002/esp.2065.

Gran, K., Paola, C., 2001. Riparian vegetation controls on braided stream dynamics. Water Resour. Res. 37, 3275–3283. http://dx.doi.org/10.1029/2000WR000203.

Grenfell, M.C., Aalto, R., Nicholas, A.P., 2012. Chute channel dynamics in large, sand-bed meandering rivers. Earth Surf. Process. Landf. 37, 315–331. http://dx.doi.org/10.1002/esp.2257.

Grenfell, M.C., Nicholas, A.P., Aalto, R., 2014. Mediative adjustment of river dynamics: the role of chute channels in tropical sand-bed meandering rivers. Sediment. Geol. 301, 93–106. http://dx.doi.org/10.1016/j.sedgeo.2013.06.007.

Hall, P., 2004. Alternating bar instabilities in unsteady channel flows over erodible beds. J. Fluid Mech. 499, 49–73. http://dx.doi.org/10.1017/S0022112003006219.

Hasegawa, K., 1981. Bank-erosion discharge based on a non-equilibrium theory. Trans. Jpn Soc. Civ. Eng. 316, 37–50.

Hooke, J.M., 2004. Cutoffs galore!: occurrence and causes of multiple cutoffs on a meandering river. Geomorphology 61, 225–238. http://dx.doi.org/10.1016/j.geomorph.2003.12.006.

Hooke, J.M., 2007. Spatial variability, mechanisms and propagation of change in an active meandering river. Sedimentology Geomorphology 84, 277–296. http://dx.doi.org/10.1016/j.geomorph.2006.06.005.

Howard, A.D., 1996. Modelling channel evolution and floodplain morphology. In: Anderson, M.G., Kochel, V.R., Patton, R.C. (Eds.), Floodplain Processes. Wiley, Chichester, UK, pp. 15–62.

Howard, A.D., Knutson, T.R., 1984. Sufficient conditions for river meandering: a simulation approach. Water Resour. Res. 20, 1659–1667. http://dx.doi.org/10.1029/WR020i011p01659.

Ikeda, S., Parker, G., Sawai, K., 1981. Bend theory of river meanders. Part 1. Linear development. J. Fluid Mech. 112, 363–377. http://dx.doi.org/10.1017/S0022112081000451.

Iwasaki, T., Shimizu, Y., Kimura, I., 2015. Numerical simulation of bar and bank erosion in a vegetated floodplain: A case study in the Otofuke River. Adv. Water Resour. 2015. http://dx.doi.org/10.1016/j.advwatres.2015.02.001 (accepted for publication).

Jang, C.L., Shimizu, Y., 2005. Numerical simulation of relatively wide, shallow channels with erodible banks. J. Hydraul. Eng. 131, 565–575. http://dx.doi.org/10.1061/(ASCE)0733-9429(2005)131:7(565).

Johannesson, H., Parker, G., 1989. Linear theory of river meanders. In: Ikeda, S., Parker, G. (Eds.), River Meandering 12. American Geophysical Union, Washington D.C., pp. 181–213.

Kleinhans, M.G., Van den Berg, J.H., 2011. River channel and bar patterns explained and predicted by an empirical and a physics-based method. Earth Surf. Process. Landf. 36, 721–738. http://dx.doi.org/10.1002/esp.2090.

Kleinhans, M.G., Schuurman, F., Bakx, W., Markies, H., 2009. Meandering channel dynamics in highly cohesive sediment on an intertidal mud flat in the Westerschelde estuary, the Netherlands. Geomorphology 105, 261–276. http://dx.doi.org/10.1016/j.geomorph.2008.10.005.

Lanzoni, S., Seminara, G., 2006. On the nature of meander instability. J. Geophys. Res. 111, F04006. http://dx.doi.org/10.1029/2005JF000416.

Mosselman, E., 1995. A review of mathematical models of river planform changes. Earth Surf. Process. Landf. 20, 661–670. http://dx.doi.org/10.1002/esp.3290200708.

Mosselman, E., Tubino, M., Zolezzi, G., 2006. The overdeepening theory in river morphodynamics: two decades of shifting interpretations. In: Ferreira, R.M.L., Alves, E.C.T.L., Leal, J.G.A.B., Cardoso, A.J. (Eds.), Proc. 5th IAHR Conf. River, Coastal and Estuarine Morphodynamics. Taylor & Francis, London, UK, pp. 1175–1181.

Motta, D., Abad, J.D., Langedoen, E.J., Garcia, M.H., 2012. The effects of floodplain soil heterogeneity on meander planform shape. Water Resour. Res. 48, W09518. http://dx.doi.org/10.1029/2011WR011601.

Nicholas, A.P., 2013. Modelling the continuum of river channel patterns. Earth Surf. Process. Landf. 38, 1187–1196. http://dx.doi.org/10.1002/esp.3431.

Olesen, K.W., 1983. Alternate bars in and meandering of alluvial rivers. In: Elliott, C.M. (Ed.), River Meandering, Proc. of the Conf. Rivers '83, New Orleans, Louisiana, US. ASCE, New York, US, pp. 873–884.

Olsen, N.R., 2003. Three-dimensional cfd modelling of self-forming meandering channel. J. Hydraul. Eng. 129, 366–372. http://dx.doi.org/10.1061/(ASCE)07339429(2003)129:5(366).

Parker, G., 1976. On the cause and characteristic scales of meandering and braiding in rivers. J. Fluid Mech. 76, 457–479. http://dx.doi.org/10.1017/S0022112076000748.

Parker, G., Andrews, E.D., 1986. On the time development of meander bends. J. Fluid Mech. 162, 139–156. http://dx.doi.org/10.1017/S0022112086001970.

Parker, G., Shimizu, Y., Wilkerson, G.V., Eke, E.C., Abad, J.D., Lauer, J.W., Paola, C., Dietrich, W.E., Voller, V.R., 2011. A new framework for modeling the migration of meandering rivers. Earth Surf. Process. Landf. 36, 70–86. http://dx.doi.org/10.1002/esp.2113.

Roelvink, J.A., 2006. Coastal morphodynamic evolution techniques. Coast. Eng. 53, 277–287. http://dx.doi.org/10.1016/j.coastaleng.2005.10.015.

Rominger, J.T., Lightbody, A.F., Nepf, H.M., 2010. Effects of added vegetation on sand bar stability and stream hydrodynamics. J. Hydraul. Eng. 136, 994–1002. http://dx.doi.org/10.1061/(ASCE)HY.1943-7900.0000215.

Sarker, S.K., Basumallick, S., 1968. Morphology, structure, and evolution of a channel island in the Barakar River, Barakar, West Bengal. J. Sediment. Petrol. 38, 747–754. http://dx.doi.org/10.1306/74D71A5F-2B21-11D7-8648000102C1865D.

Schielen, R., Doelman, A., De Swart, H.E., 1993. On the nonlinear dynamics of free bars in straight channels. J. Fluid Mech. 252, 325–356. http://dx.doi.org/10.1017/S0022112093003787.

Schuurman, F., Kleinhans, M.G., 2015. Bar dynamics and bifurcation evolution in a modelled braided sand-bed river. Earth Surf. Process. Landf. 40, 1318–1333. http://dx.doi.org/10.1002/esp.3722.

Schuurman, F., Kleinhans, M.G., Marra, W.A., 2013. Physics-based modeling of large braided sand-bed rivers: bar pattern formation, dynamics, and sensitivity. J. Geophys. Res. 118, 2509–2527. http://dx.doi.org/10.1002/2013JF002896.

Seminara, G., Tubino, M., 1989. Alternate bars and meandering: free, forced and mixed interactions. In: Ikeda, S., Parker, G. (Eds.), River Meandering 12. American Geophysical Union, Washington D.C., pp. 267–320.

Struiksma, N., Crosato, A., 1989. Analysis of a 2-d bed topography model for rivers. In: Ikeda, S., Parker, G. (Eds.), River Meandering 12. American Geophysical Union, Washington D.C., pp. 153–180.

Struiksma, N., Olesen, K., Flokstra, C., De Vriend, H., 1985. Bed deformation in curved alluvial channels. J. Hydraul. Res. 23, 57–79. http://dx.doi.org/10.1080/00221688509499377.

Sun, T., Meakin, P., Jossang, T., Schwarz, K., 1996. A simulation model for meandering rivers. Water Resour. Res. 32, 2937–2954. http://dx.doi.org/10.1029/96WR900998.

Tal, M., Paola, C., 2010. Effects of vegetation on channel morphodynamics: results and insights from laboratory experiments. Earth Surf. Process. Landf. 35, 1014–1028. http://dx.doi.org/10.1002/esp.1908.

Talmon, A.M., Struiksma, N., Van Mierlo, M.C.L.M., 1995. Laboratory measurements of the direction of sediment transport on transverse alluvial-bed slopes. J. Hydraul. Res. 33, 495–517. http://dx.doi.org/10.1080/00221689509498657.

Torrence, C., Compo, G.P., 1998. A practical guide to wavelet analysis. Bull. Am. Meteorol. Soc. 79, 61–78. http://dx.doi.org/10.1175/1520-0477(1998)079<0061:APGTWA>2.0.CO;2.

Tubino, M., Seminara, G., 1990. Free-forced interactions in developing meanders and suppression of free bars. J. Fluid Mech. 214, 131–159. http://dx.doi.org/10.1017/S0022112090000088.

Van de Lageweg, W.I., Van Dijk, W.M., Baar, A.W., Rutten, J., Kleinhans, M.G., 2014. Bank pull or bar push: what drives scroll-bar formation in meandering rivers? Geology 42, 319–322. http://dx.doi.org/10.1130/G35192.1.

Van Dijk, W.M., Schuurman, F., Van de Lageweg, W.I., Kleinhans, M.G., 2014. Bifurcation instability and chute cutoff development in meandering gravel-bed rivers. Geomorphology 213, 277–291. http://dx.doi.org/10.1016/j.geomorph.2014.01.018.

Van Dijk, W.M., Teske, R., Van de Lageweg, W.I., Kleinhans, M.G., 2013a. Effects of vegetation distribution on experimental river channel dynamics. *Water Resour.* Res. 49, 7558–7574. http://dx.doi.org/10.1002/2013WR013574.

Van Dijk, W.M., Van de Lageweg, W.I., Kleinhans, M.G., 2012. Experimental meandering river with chute cutoffs. J. Geophys. Res. 117, F03023. http://dx.doi.org/10.1029/2011JF002314.

Van Dijk, W.M., Van de Lageweg, W.I., Kleinhans, M.G., 2013b. Formation of a cohesive floodplain in a dynamic experimental meandering river. Earth Surf. Process. Landf. 38, 1550–1565. http://dx.doi.org/10.1002/esp.3400.

Whiting, P.J., Dietrich, W.E., 1993. Experimental constraints on bar migration through bends: implications for meander wavelength selection. Water Resour. Res. 29, 1091–1102. http://dx.doi.org/10.1029/92WR02356.